# Mantle plume migration ?

Chuansong He[1]

[1]Institute of Geophysics China Earthquake Adminstration

November 22, 2022

**Abstract**

The stagnation and dehydration of the Pacific Plate slab in the mantle transition zone are widely accepted to have resulted in Mesozoic and Cenozoic volcanic activities and the formation of the Songliao Basin in NE China. However, this notion has been challenged by recent seismic studies. Alternatively, a mantle plume may have generated large-scale volcanism and led to the formation of the Songliao Basin. In this study, a detailed analysis involving common conversion point (CCP) stacking of receiver functions was carried out. The results reveal a significantly deepened region of the 410 km discontinuity and an elevated region of the 660 km discontinuity in the centre of NE China (or the Songliao Basin). The combination of these results with those of a previous study suggests that an upwelling mantle plume was located under the centre of the Songliao Basin in the Mesozoic. Furthermore, the distinctive structure of the mantle transition zone (MTZ) beneath the southern part of the Songliao Basin identified in this study is correspond to mantle plume upwelling (a mushroom-shaped low-velocity anomaly), which may be related to the Changbaishan volcanic activities in the Cenozoic.

## Mantle plume migration ?

Chuansong He11* hechuansong@aliyun.com

Institute of Geophysics, China Earthquake Administration, Beijing 100081, China

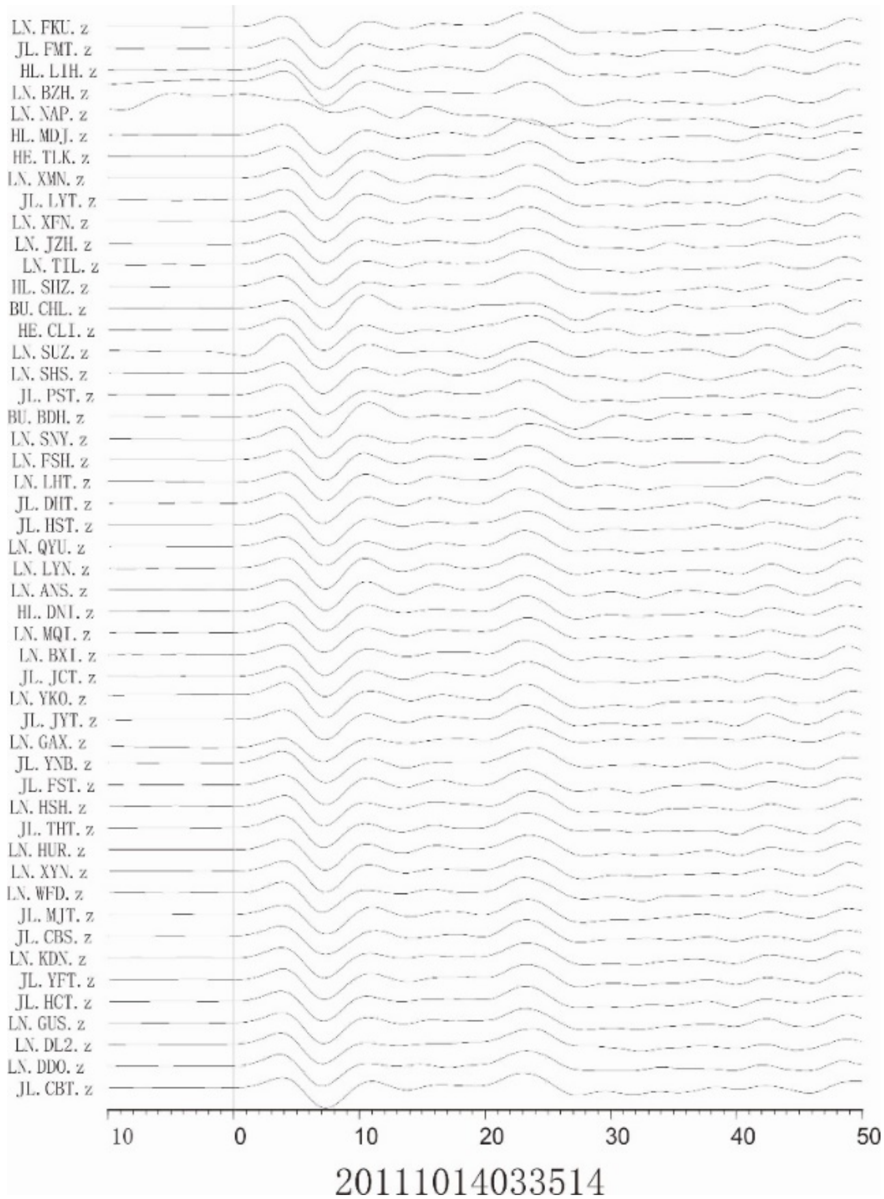


Figure S1. Vertical component of events (2011014033514) recorded by the permanent seismic stations. Horizontal coordinate: Second.

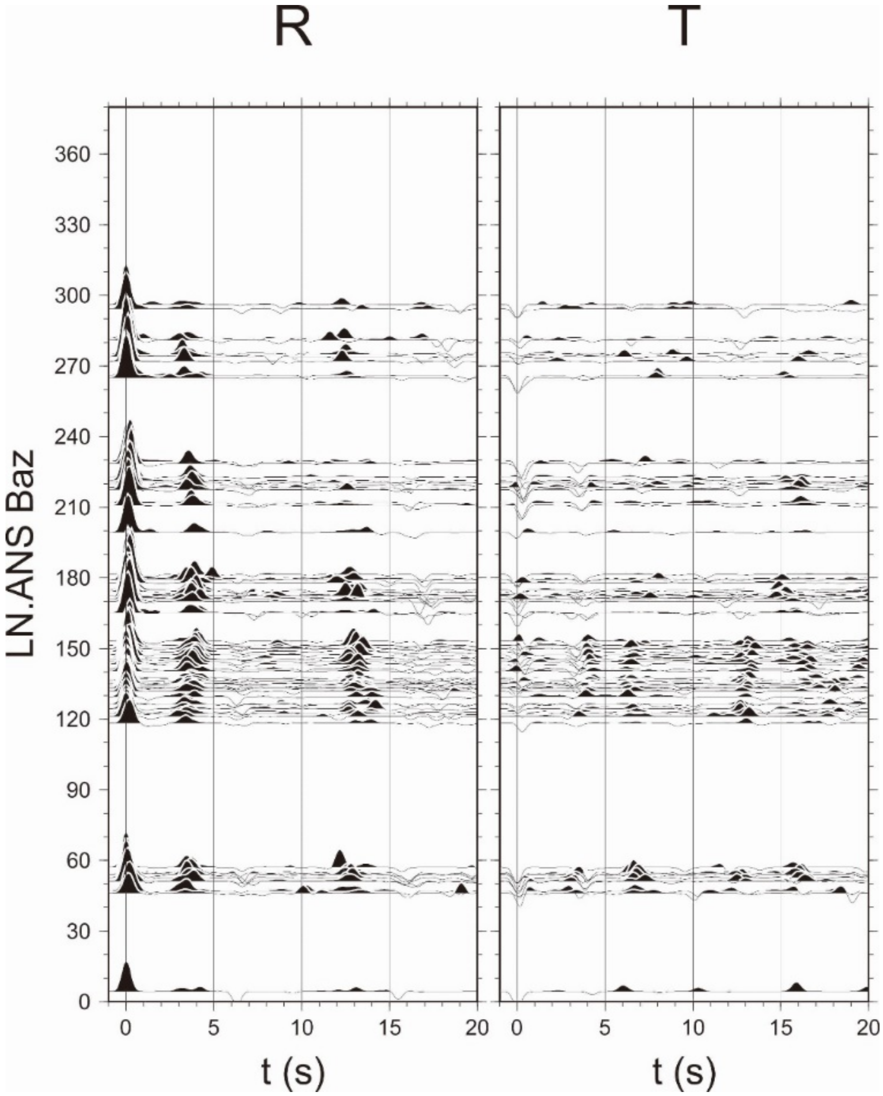


Figure S2. Receiver function recorded by LN.ANS seismic station. Left panel: R-receiver function, right panel: T-receiver function.

11

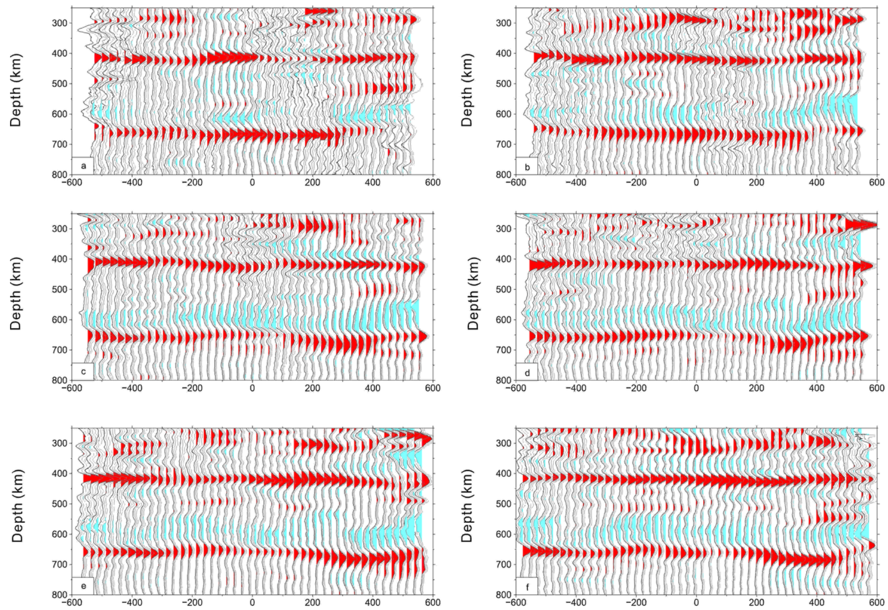


Fig. S3. Example for the bootstrap resampling method (a-f profiles). Horizontal coordinate: km.

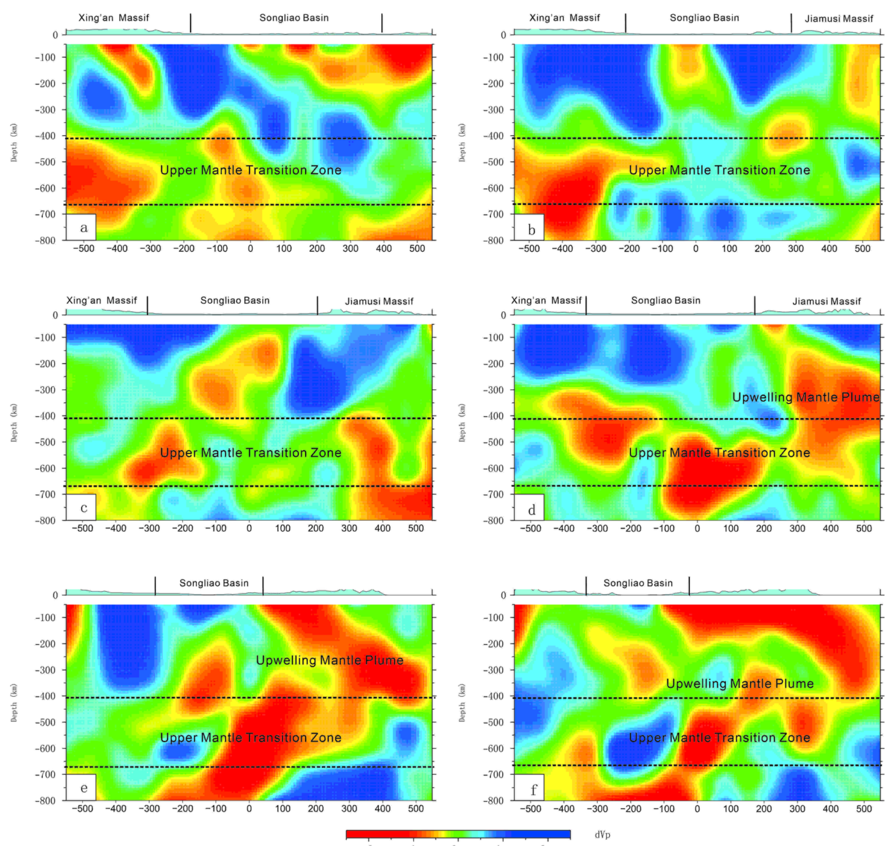


Fig. S4. P-wave velocity perturbation (the profiles location, please see Fig. 1) (He and Santosh, 2016).

Horizontal coordinate: km. The blue dotted lines are 410 and 660 km discontinuities, respectively. The MTZ bounded by the 410 and 660 km discontinuities.

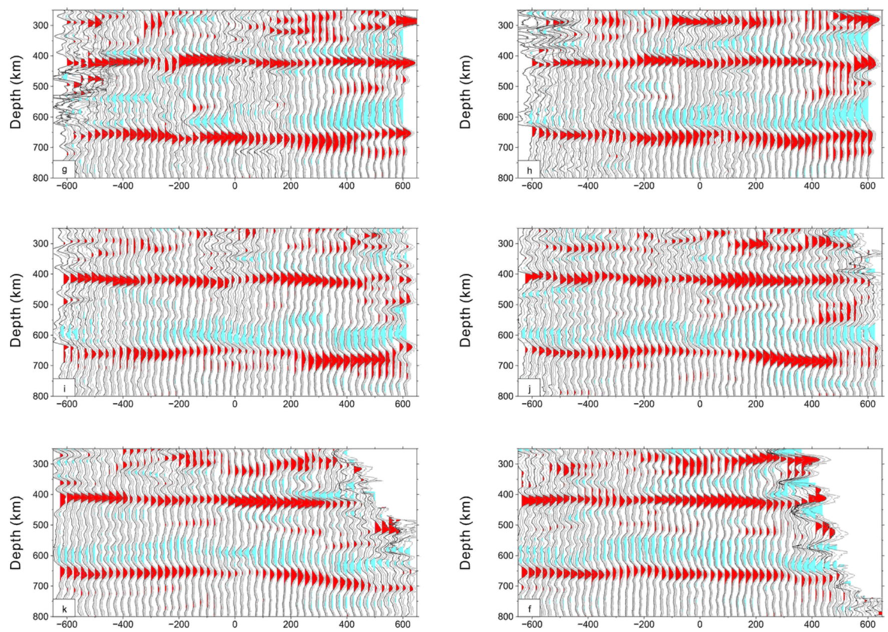


Fig. S5. Example for the bootstrap resampling method (g-l profiles). Horizontal coordinate: km.

# Mantle plume migration ?

Chuansong He[1]

[1]Institute of Geophysics, China Earthquake Administration, Beijing 100081, China

**Abstract:** The stagnation and dehydration of the Pacific Plate slab in the mantle transition zone are widely accepted to have resulted in Mesozoic and Cenozoic volcanic activities and the formation of the Songliao Basin in NE China. However, this notion has been challenged by recent seismic studies. Alternatively, a mantle plume may have generated large-scale volcanism and led to the formation of the Songliao Basin. In this study, a detailed analysis involving common conversion point (CCP) stacking of receiver functions was carried out. The results reveal a significantly deepened region of the 410 km discontinuity and an elevated region of the 660 km discontinuity in the centre of NE China (or the Songliao Basin). The combination of these results with those of a previous study suggests that an upwelling mantle plume was located under the centre of the Songliao Basin in the Mesozoic. Furthermore, the distinctive structure of the mantle transition zone (MTZ) beneath the southern part of the Songliao Basin identified in this study is correspond to mantle plume upwelling (a mushroom-shaped low-velocity anomaly), which may be related to the Changbaishan volcanic activities in the Cenozoic.

[1] email:hechuansong@aliyun.com

Key words: Upwelling mantle plume; 410 km discontinuity; 660 km discontinuity; CCP stacking of receiver function; Songliao Basin; NE China.

## 1. Introduction

NE China, which includes the Xingan Massif, Jiamusi Massif and Songliao Massif, is located on the eastern margin of the Eurasian continent, is part of the Central Asian Orogenic Belt and is bounded by the Siberian craton to the north and the North China Craton to the south (Fig. 1). This region experienced the final closure of the Palaeo-Asian Ocean and the westward subduction of the Palaeo-Pacific Plate from the late Palaeozoic to the early Mesozoic (Tang et al., 2018; Xiao et al., 2015; Ryu and Lee, 2017; Wang et al., 2019; Sun et al., 2018), as well as intense Mesozoic-Cenozoic volcanism and the establishment of the Songliao Basin.

Since the 1990s, the concept of a stagnant slab in the mantle transition zone (MTZ) (MTZ is bounded by the 410 and 660 km discontinuities) generated by the subducted Pacific Plate has been widely accepted, and dehydration of this stagnant slab may be related to extensive volcanism in the Mesozoic and Cenozoic (Zhao et al., 1994; Zhao et al., 2019; Maruyama et al., 2009; Chen and Faccenda, 2019). This process is proposed to have resulted in related metallogenesis, tectonic extension, rifting processes and formation of the Songliao Basin (Wu et al., 2003; Bao and Niu, 2017; Yang et al., 2017).

However, whether the volcanism, rifting processes and Songliao Basin formation can be attributed to a stagnant slab in the MTZ is a matter of debate.

Recently, a number of tomographic and receiver function studies have been carried out in NE China and nearby regions (Ai et al., 2003; Li and Yuan, 200; Lei and Zhao, 2005; Gao et al., 2010; Tang et al., 2014; He et al., 2014; He and Santosh, 2016; Liu et al., 2017; Zhang et al., 2019; Fan et al., 2020; Kim et al., 2016; Zhu et al., 2019; Lu et al., 2020; Sun et al., 2020). Among them, some tomographic studies failed to observe significant high-velocity anomalies (or a stagnant slab) in the MTZ (e.g., Tang et al., 2014; He and Santosh, 2016). Additionally, receiver function studies have defined the topographies of the upper mantle discontinuities associated with thermal upwelling (He et al., 2014; He, 2019). However, common conversion point (CCP) stacking of receiver functions in previous studies used a single 1-D or pseudo 3-D velocity model (He et al., 2014; He et al., 2019); moreover, it does not consider the effect of S-wave velocity and slowness (He et al., 2014; He et al., 2019). Therefore, previous studies cannot define the detailed topographies of the 410 and 660 km discontinuities, which are a key indicator of the temperature variation in the upper mantle and closely related to the thermal upwelling of the mantle (Foulger, 2012).

In this study, the detailed topographies of the 410 and 660 km discontinuities were inferred from the CCP stacking of receiver functions. A 3-D global velocity model (Lu et al., 2019) and a local velocity model (He and Santosh, 2016) are used to correct the apparent depths of the 410 and 660 km discontinuities. The results indicate that there are significant variations in the 410 and 660 km discontinuities beneath the centre of NE China (specifically, the Songliao Basin) and its southern part, which may be related to mantle plume upwelling.

## 2. Method and data

In the study region, a total of 1220 teleseismic events were extracted from 127 permanent seismic stations recorded from 2007 to 2014, and 282 teleseismic events were collected from 148 temporary seismic stations (Fig. 1). The events were limited to Ms >6.0, and the earthquake epicentral distances ranged from 30° to 90° for individual event-station pairs. A Butterworth bandpass filter between 0.05 and 1 Hz was applied to the raw record, which was cut from 15 *s* before to 120 *s* after the P-wave arrival. To obtain a high signal-to-noise ratio for all events, the waveform cross-correlation technique (VanDecar and Crosson, 1990) was used to select consistent raw data (for example, please see Fig. S1). In total, 21627 high-quality receiver functions were calculated by a modified frequency-domain deconvolution with a 1 *Hz* Gaussian filter and 0.01 water level (Langston, 1979; Zhu and Kannamori, 2000) (for example, please see Fig. S2).

The topographies of the 410 and 660 km discontinuities in the study region are defined by the CCP technique (VanDecar and Crosson, 1997; Eagar et al., 2010; Zhu, 2000). The spherical coordinates used to calculate Ps–P differential time $T_{Ps}$ (Eagar et al., 2010):

$$T_{Ps} = \sum_i^N \left( \sqrt{\left(\frac{R_i}{V_{Si}}\right) - p_{P_s}^2} - \sqrt{\left(\frac{R_i}{V_{Pi}}\right) - p_P^2} \right) \frac{\Delta r}{R_i} \quad (1)$$

whered $p_{Ps}$ and $p_P$ are the ray parameters of the direct Ps and P phases, respectively and $V_{Pi}$ and $V_{Si}$ are the P- and S-wave velocities, respectively, in the *i*th layer. $R_i$ and $\Delta r$ are the Earth's semidiameter at each *i*th depth shell ($r_i$) and depth interval, respectively. To ensure the reliability of the results, a 3-D global P- and S-wave velocity model by Lu et al. (2019) and local 3-D velocity model in the area by He and Santosh (2016) are employed to remove the velocity heterogeneity effects in the upper mantle. The Ps-P differential times in the 3-D model were presented as follows:

$$T_{Ps3D} = T_{Ps} + \Delta T \quad (2)$$

where $\Delta T$ is related to the 3-D velocity velocity perturbations or the travel time correction

A depth interval of 1 km and a lateral grid interval of 0.5° were designed in the grid of CCP stacking of receiver functions, and a radius (or bin) of 75 km used to search for the migrated receiver functions (Xu et al., 2018). In each bin, a total of 2000 resampling iterations of the bootstrap resampling are employed to calculate the standard deviation and mean value.

## 3. Results

In Fig. 2, there are no obvious changes in the 410 and 660 km discontinuities in profiles a and b (Fig. 2 a, b). In contrast, at the centres of profiles c and d, the 410 km discontinuity shows significant deepening by approximately 15 km (Fig. 2c, d; blue rectangle), whereas the 660 km discontinuity exhibits significant shallowing by approximately 20 km (Fig. 2 c). Previous receiver function studies show results similar to those of the c profile (He, 2019); however, the 410 and 660 km discontinuities of the d profile did not have any signature of the anomaly (He, 2019). The 660 km discontinuity appears topographically elevated in the centres of profiles e and f (Fig. 2 e, f; yellow rectangle).

To further clarify the relationship between the upwelling mantle plume and the upper mantle discontinuities, the P-wave velocity perturbation profiles (He and Santosh, 2016) (e and f profiles of Fig. S4) are overlain on the CCP stacking profiles of the receiver functions (e and f profiles of Fig. 2) (Fig. 3). The results indicate that the elevated location of the 660 km discontinuity correspond well to that of an upwelling mantle plume (Fig. 3e, f; white rectangle region).

Additionally, 6 CCP stacking profiles (g-l) of receiver functions were created (Fig. 4; for the locations of the profiles, please see Fig. 1). The images from the CCP stacking of receiver functions show a deepened region for the 410 km discontinuity and an elevated region for the 660 km discontinuity at the centres of the profiles (Songliao Basin) (Fig. 4 i, j, regions indicated by the blue rectangles). An elevated region for the 660 km discontinuity at the centres of the k and l profiles, which corresponds to the location of the upwelling mantle plume (Fig. 4 k, l, regions indicated by the yellow rectangles).

The depths of the 410 and 660 km discontinuities and the MTZ thickness in the study region have been extracted (Fig. 5 e, f and g). The results show a deepened region for the 410 km discontinuity (Fig. 5e, white circle region) and an elevated region for the 660 km discontinuity (Fig. 5 f, white circle region), resulting in thinning of the MTZ thickness (Fig. 5 g, white circle region) in the centre of NE China (specifically, the Songliao Basin). At southern part of the Songliao Basin, the 410 km discontinuity appears to be relatively deep, with slight shallowing in a localized region (Fig. 5e, green circle region); the 660 km discontinuity appears to be relatively shallow (Fig. 5f, green circle region); and the MTZ is therefore relatively thin (Fig. 5g, green circle region).

Meanwhile, a local 3-D velocity model (He and Santosh, 2016) was used to correct the CCP stacking results of the receiver function, and the S-wave velocity was calculated from the Vp/Vs ratio of the AK135 velocity model (Kennett et al., 1995). The results indicate that the topographies of the 410 and 660 km discontinuities and the MTZ thickness beneath the centre of NE China and its southern part inferred from this model are basically consistent with those from the 3-D global P- and S-wave velocity model (Lu et al., 2019).

## 4. Discussion

### 4.1 Mesozoic mantle plume and migration of the mantle plume

Receiver functions are the most popular tool for investigating the 410 and 660 km discontinuities and the structure of the MTZ (Agius et al., 2017). Imaging the topographies of the 410 and 660 km discontinuities and the MTZ thickness plays a key role in understanding the thermal conditions of the MTZ (He et al., 2014; Zhang et al., 2019), thereby providing an indication of mantle convection within the Earth (Foulger, 2012).

Based on seismic imaging and mineral physical experiments (Katsura and Ito,1989; Ito and Takahashi, 1989; Ringwood, 1975; Deuss, 2006), the 410 discontinuity, which exhibits a positive Clapeyron slope, involves the phase transition of olivine to wadsleyite (Helffrich, 2000; Kawai et al., 2013; Jenkins et al., 2016; Frost, 2008), and the temperature increases with increasing depth. In contrast, the 660 discontinuity, which exhibits a negative Clapeyron slope, is likely associated with the phase transition of ringwoodite to perovskite and magnesiowüsite (Helffrich, 2000; Kawai et al., 2013; Jenkins et al., 2016), and the temperature increases with decreasing depth.

Mantle plumes are expected to affect the topographies of the 410 and 660 km discontinuities and the MTZ thickness because they pass through the MTZ and have higher temperatures than the surrounding mantle (Deuss, 2007). Consequently, mantle plumes might deepen the topography of the 410 km discontinuity (deepening 15-20 km) and elevate the topography of the 660 km discontinuity, resulting in MTZ thinning (Shen et al., 2002). Thus, the results identified in this study show that the features of the 410 and 660 km discontinuities and the MTZ in the centre of NE China (specifically, the Songliao Basin) may be related to mantle plume upwelling (Fig. 5, Fig. 6).

Upwelling mantle plumes can generate lower crustal underplating (Pirajno, 2007), which led to high Vp/Vs ratio in the crust (or lower crust). A previous receiver function (He et al., 2016) study concluded that high Vp/Vs ratios (possibly related to lower crustal magmatic underplating induced by upwelling mantle plume) and crustal thinning exists in the centre of NE China (the Songliao Basin) (Fig. 7a, b). The large areas of continental rift basalt that formed in NE China during the Late Jurassic to Late Cretaceous are associated with an upwelling mantle plume (Ren et al., 2002). Geological studies have also found that basalts erupted from more than 590 volcanoes across an area of approximately 50,000 $km^2$ in the Songliao Basin in the Mesozoic (Liu et al., 2001), which may be related to upwelling mantle plume; in contrast, volcanism was relatively rare on the margins of the Songliao Basin in the Mesozoic (Liu et al., 2001). These results support the interpretation that the MTZ structure beneath NE China (specifically, the Songliao Basin) may be a relic of Mesozoic mantle plume upwelling, which might be related to the formation of the Songliao Basin (He et al., 2014).

However, tomographic data do not reveal a relic of mantle plume upwelling beneath the Songliao Basin; in contrast, tomographic data define a relic of mantle plume upwelling under the southern margin of the Songliao Basin (Fig. S4 e, f) (Tang et al., 2014; He and Santosh, 2016). Relics of upwelling mantle plumes can be retained for several million to several billion years (Burk and Torsvik, 2004; Chang and Van der Lee, 2011). Thus, the relic of the upwelling Mesozoic mantle plume should not have disappeared. Therefore, it is proposed that the upwelling mantle plume beneath the Songliao Basin may have migrated to the current position defined by tomography (He and Santosh, 2016) (Fig. 8). Based on the results identified in the tomography (He and Santosh, 2016) (Fig. 3), it is suggested that the upwelling mantle plume might occur title from west to east during the migration process.

Volcanism showed a spatial shift from the centre of the Songliao Basin to the edges of the basin, and the products of this volcanism decrease in age from west to the east in NE China (Sun et al., 2020), which may be related to the migration and tilte of the upwelling mantle plume. Recent seismic studies have reported that the plume beneath Hawaii has also migrated rather than remaining stationary (Torsvik et al., 2017).

**4.2. Cenozoic mantle plume**

Since approximately 2.77 Ma, the CBS, located on the eastern margin of the Songliao Basin, has produced a series of eruptions (Wang et al., 2003) that have affected an area with a diameter of 300 km (Kuritani et al., 1982). The distinctive structure of the MTZ (Fig. 2 e, f, Fig. 5 and Fig. 6) identified in this study might be indicative of an upwelling mantle plume at the southern part of the Songliao Basin (Fig. 8); moreover, the surface projection of the upwelling mantle plume identified by tomography (He and Santosh, 2016) corresponds to the CBS (Fig. 1; Fig. S4, profile e and f). Therefore, mantle plume upwelling may have contributed to the Cenozoic volcanism of the CBS (Turcotte and Schubert, 1982). Rare earth element (REE) studies indicate that the magmatism of the CBS is related to a mantle source and might be associated with mantle plume upwelling in the Cenozoic (Fan et al., 2007; Basu et al., 1991).

## 5. Conclusions

The results identified in this study indicate that a relic of an upwelling mantle plume exists beneath the Songliao Basin, which may be related to large-scale volcanism and Songliao Basin formation in the Mesozoic. There is a possibility that the Mesozoic plume may have migrated to the southern part of the Songliao Basin and occured title.

A deepened region of the 410 km discontinuity and an elevated region of the 660 km discontinuity as well as the thinning of the MTZ in the southern part of the Songliao Basin identified in this study correspond to the mushroom-shaped low-velocity anomaly (or upwelling mantle plume) identified in the previous topographies. Its surface project correspond to the CBS, which implied that mantle plume upwelling might result in the formation of the Changbaishan volcanism in the Cenozoic.

## Acknowledgements

Thanks to the National Key RandD Plan of China (2017YFC601406), the Data Management Centre of the China National Seismic Network at the Institute of Geophysics and the China Earthquake Networks Centre. The data involved in the CCP stacking of receiver functions can be accessed via https://doi.org/10.5281/zenodo.3762789.

## References

Agius, M.R., Rychert, C.A., Harmon, N. and Laske, G. .2017. Mapping the mantle transition zone beneath Hawaii from Ps receiver functions: Evidence for a hot plume and cold mantle downwellings. *Earth Planet. Sci. Lett.,* **474**, 226-236.

Ai, Y.S., Zheng, T.Y., Xu, W.W., He, Y.M. and Dong, D.A .2003. A complex 660 km discontinuity beneath northeast China. *Earth Planet. Sci. Lett.,* **212**, 63-71.

Bao, Y. and Niu, F. 2017. Constraining sedimentary structure using frequency dependent P wave particle motion: A case study of the Songliao Basin in NE China. *J. Geophys. Res.,* **122**, 9083-9094.

Basu, A.R., Wang, J.W., Huang, W.K., Xie, G.H. and Tatsumoto, M. 1991. Major element, REE, and Pb, Nd and Sr isotopic geochemistry of Cenozoic volcanic rocks of eastern China: implications for their origin from suboceanic-type mantle reservoirs. *Earth*

*Planet. Sci. Lett.,* **105**, 149-169.

Burke, K. and Torsvik, T.H. 2004. Derivation of Large Igneous Provinces of the past 200 million years from long-term heterogeneities in the deep mantle. *Earth Planet. Sci. Lett.,* **227**, 531-538.

Chang, S.J. and Van der Lee, S. 2011. Mantle plumes and associated flow beneath Arabia and East Africa. *Earth Planet. Sci. Lett.,* **302**, 448-454.

Chen, L. and Faccenda, M. 2019. Subduction‐induced upwelling of a hydrous transition zone: Implications for the Cenozoic magmatism in northeast China. *J. Geophys. Res.,* **124**, 11,489-11,504.

Deuss, A. 2007. Seismic observations of transition-zone discontinuities beneath hotspot locations. *Geol. Soc. Am. Spec. Pap.,* **430**, 121-136.

Deuss, A., Redfern, S.A.T., Chambers, K. and Woodhouse, J. H. 2006. The nature of the 660‐kilometer discontinuity in Earth's mantle from global seismic observations of PP precursors. *Science,* **311**, 198-201.

Dueker, K.G. and Sheehan, A.F. 1997. Mantle discontinuity structure from midpoint stacks of converted P to S waves across the Yellowstone hotspot track. *J. Geophys. Res.,* **102**, 8313-8327.

Eagar, K.C., Fouch, M.J. and James, D.E. 2010. Receiver function imaging of upper mantle complexity beneath the Pacific Northwest, United States. *Earth Planet. Sci. Lett.,* **297**, 141-153.

Efron, B. and Tibshirani, R.B.1986. Bootstrap methods for standard errors, confidence intervals, and other measures of statistical accuracy. *Stat. Sci*., **1**, 54-75.

Fan, Q.C., Sui, J.l., Wang, T.H., Li, N. and Sun, Q. 2007. History of Volcanic Activity, Magma Evolution and Eruptive Mechanisms of the Changbai Volcanic Province. *Geol. J. China Univ.,* **13,** 175-190 (in Chinese with English abstract).

Fan, X., Chen, Q.F., Legendre, C.P. and Guo, Z. 2020. Intraplate volcanism and regional geodynamics in NE Asia revealed by anisotropic Rayleigh - wave tomography. *Geophys. Res. Lett.,* **47**, e2019GL085623.

Frost, D. J. 2008. The upper mantle and transition zone. *Elements* 4, 171-176.

Foulger, G.R. 2012. Are ‘hot spots’ hot spots?. *J. Geodyn.*, *58*, 1-28.

Gao, Y., Suetsugu, D., Fukaob, Y., Obayashib, M., Shi, Y.T., Liu, R.F. 2010. Seismic discontinuities in the mantle transition zone and at the top of the lower mantle beneath eastern China and Korea: Influence of the stagnant Pacific slab. *Phys. Earth Planet. Inter.,* **183**, 288-295.

He, C.S. 2019. Evidence for an upwelling mantle plume beneath the Songliao Basin, Northeast China. *Phys. Earth Planet. Inter.,* **297**, 106316.

He, C.S., Dong, S.W., Chen, X.H., Santosh, M. and Niu, S.Y. 2014. Seisic evidence for plume-induced rifting in the Songliao basin of Northeast China. *Tectonophysics* **627**, 171-181.

He, C.S. and Santosh, M. 2016. Seismic tomographic evidence for upwelling mantle plume in NE China. Phys. *Earth Planet. Inter.,* **254**, 37-45.

Helffrich, G. 2000. Topography of the transition zone seismic discontinuities. *Rev. Geophy.,* **38**, 141-158.

Ito, E. and Takahashi, E. 1989. Postspinel transformations in the system

Mg2SiO4-Fe2Si04 and some geophysical implications. *J. Geophys. Res.,* **94**, 10637-10646.

Jenkins, J., Cottaar, S., White, R.S. and Deuss. A. 2016. Depressed mantle discontinuities beneath Iceland: Evidence of a garnet controlled 660 km discontinuity?. *Earth Planet. Sci. Lett.,* **433**, 159-168.

Katsura, T. and Ito, E. 1989. The system Mg2SiO4-Fe2SiO4 at high pressures and temperatures: Precise determination of stabilities of olivine, modified spinel, and spinel. *J. Geophys. Res.,* **94**, 15663-15670.

Kawai, K., Yamamoto, S., Tsuchiya, T. and Maruyama, S. 2013. The second continent: Existence of granitic continental materials around the bottom of the mantle transition zone. *Geosci. Front.,* **4**, 1-6.

Kennett, B.L.N., Engdahl, E.R. and Buland, R. 1995. Constraints on seismic velocities in the Earth from traveltimes. *Geophys. J. Int.,* **122**, 108-124.

Kim, S., Tkalčić, H., Rhie, J. and Chen, Y. 2016. Intraplate volcanism controlled by back-arc and continental structures in NE Asia inferred from transdimensional Bayesian ambient noise tomography. *Geophys. Res. Lett.,* **43**, 8390-8398.

Kuritani, T., Ohtani, E. and Kimura, J.I. 2011. Intensive hydration of themantle transition zone beneath China caused by ancient slab stagnation. *Nat. Geosci.,* **4**, 713-716.

Maruyama, S., Hasegawa, A., Santosh, M., Kogiso, T., Omori, S., Nakamura, H., Kawai, K., Zhao, D. 2009. The dynamics of big mantle wedge, magma factory, and metamorphic-metasomatic factory in subduction zones. *Gondwana Res.,* **16**, 414-430.

Langston, C.A. 1979. Structure under Mount Rainier, Washington, inferred from teleseismic body waves. *J. Geophys. Res.,* **84**, 4749-4762.

Lei, J.S. and Zhao, D. 2005. P-wave tomography and origin of the Changbai intraplate volcano in Northeast Asia. *Tectonophysics,* **397**, 281-295.

Li, X.Q. and Yuan, X.H. 2003. Receiver functions in northeast China - implications for slab penetration into the lower mantle in northwest Pacific subduction zone. *Earth Planet. Sci. Lett.,* **216**, 679-691.

Liu, J., Han, J. and Fyfe, W.S. 2001. Cenozoic episodic volcanism and continental rift-ing in northeast China and possible link to Japan Sea development as revealed from K–Ar geochronology. *Tectonophysics,* **339**, 385-401.

Liu, Y.N., Niu, F.L., Chen, M. and Yang, W.C. 2017. 3-D crustal and uppermost mantle structure beneath NE China revealed by ambient noise adjoint tomography. *Earth Planet. Sci. Lett.,* **461**, 20-29.

Lu, C., Grand, S.P., Lai, H. and Garnero, E.J. 2019. TX2019slab: A New P and S Tomography Model Incorporating Subducting Slabs. *J. Geophys. Res*., **124**, 11549-11567.

Lu, M., Lei, J., Zhao, D., Ai, Y., Xu, X. and Zhang, G. 2020. SKS splitting measurements in NE China: New insights into the Wudalianchi intraplate volcanism and mantle dynamics. *J. Geophys. Res.,* **125**, e2019JB018575.

Pilidou, S., Priestley, K., Debayle, E. and Gudmundsson, Ó. 2005. Rayleigh wave tomography in the North Atlantic: high resolution images of the Iceland, Azores and Eifel mantle plumes. *Lithos, 79,* 453-474.

Phillips, E.H., Sims, K. W.W., Blichert-Toft, J., Aster, R.C., Gaetani, G.A., Kyle, P.R., Wallace, P.J. and Rasmussen, D.J. 2018. The nature and evolution of mantle upwelling at Ross Island, Antarctica, with implications for the source of HIMU lavas. *Earth Planet. Sci. Lett., 498*, 38-53.

Pirajno, F. 2007. Ancient to modern earth: the role of mantle plume in the making of continental crust: Earth's Oldest Rocks, edited by Kranendonk, M.J.V., Smithies, R.H., and Bennett, V.C., Developments in Precambrian Geology, v.15 (K.C. Condie, Series Editor).

Ren, J.Y., Tamaki, K., Li, S.T. and Zhang, J.X. 2002. Late Mesozoic and Cenozoic rifting and its dynamic setting in Eastern China and adjacent areas. *Tectonophysics,* **344**, 175-205.

Ringwood, A. 1975. Composition and Petrology of the Earth's Mantle. McGraw-Hill, New York, 618.

Ryu, I.C. and Lee, C. 2017. Intracontinental mantle plume and its implications for the Cretaceous tectonic history. *Earth Planet. Sci. Lett.,* **479**, 206-218.

Shaw, A.M., Hauri, E.H., Behn, M.D., Hilton, D.R., Macpherson, C.G. and Sinton, J.M. 2012. Long-term preservation of slab signatures in the mantle inferred from hydrogen isotopes. *Nat. Geosci.,* **5**, 224-228.

Shen, Y., Solomon, S.C., . Bjarnason, I.T., Nolet, G., Morgan, W.J., Allen, R.M. Kristin, V., Jakobsdóttir, S., Stefánsson, R., Julian, B.R., Foulger, G.R. 2002. Seismic evidence for a tilted mantle plume and north-south mantle flow beneath Iceland. *Earth Planet. Sci. Lett.,* **197**, 261-272.

Sun, M., Chen, H., Milan, L. A., Wilde, S. A., Jourdan, F. and Xu, Y. 2018. Continental arc and back-arc migration in eastern NE China: New constraints on Cretaceous Paleo-Pacific subduction and rollback. *Tectonics*, **37**, 3893-3915.

Sun, M., Gao, S.S., Liu, K.H. and Fu, X.F. 2020. Upper mantle and mantle transition zone thermal and water content anomalies beneath NE Asia: Constraints from receiver function imaging of the 410 and 660km discontinuities. *Earth Planet. Sci. Lett.,* **532**, 116040.

Tang, J., Xu, W.L., Wang, F. and Ge, W.C. 2018. Subduction history of the Paleo–Pacific slab beneath Eurasian continent: Mesozoic–Paleogene magmatic records in Northeast Asia. *Sci. China-D,* **61**, 527-559.

Tang, Y., Obayashi, M., Niu, F., Grand, S.P., Chen, Y.J., Kawakatsu, H., Tanaka, S., Ning, J. and Ni, J.F. 2014. Changbaishan volcanism in NE China linked to subduction-induced mantle upwelling. *Nat. Geosci*., **7**, 470.

Torsvik, T., Doubrovine, P., Steinberger, B. Gaina, C., Spakman, W. and Domeier, M. 2017. Pacific plate motion change caused the Hawaiian-Emperor Bend. *Nat. Commun.,* **8**, 15660.

Turcotte, D. and Schubert, G. 1982. Geodynamics Applications of Continuum Physics to Geological Problems. John Wiley, New York, pp.1-449.

Tang, H.F., Kong, T., Wu, C.Z., Wang, P.J., Peng, X., Gao, Y.F., 2017. Filling Pattern of Volcanostratigraphy of Cenozoic Volcanic Rocks in the Changbaishan Area and Possible Future Eruptions. *Acta Geologica Sinica,* **91**, 1717-1732.

VanDecar, J.C. and Crosson, R.S. 1990. Determination of teleseismic relative phase arrival times using multi-channel cross-correlation and least squares. *Bull. Seismol. Soc. Am.,* **80**, 150-169.

Wang, F., Xu, W.L., Xing, K.C., Wang, Y.N., Zhang, H.H., Wu, W., Sun, C.Y. and Ge, W.C. 2019. Final closure of the Paleo–Asian Ocean and onset of subduction of Paleo-Pacific Ocean: constraints from early Mesozoic magmatism in central southern Jilin Province, NE China. *J. Geophys. Res.,* **124**, 2601-2622.

Wang, Y., Li, C., Wei, H. and Shan, X. 2003. Late Pliocene–recent tectonic setting for the Tianchi volcanic zone, Changbai Mountains, northeast China. J*. Asian Earth Sci.,* **21**, 1159-1170.

Wu, F.Y., Ge, W.C., Sun, D.Y. and Guo, C.L. 2003. Discussions on the lithospheric thinning in eastern China. *Earth Sci. Front.,* **10**, 51-60 (in Chinese with English abstract).

Xiao W.J., Windley, B.F., Sun, S., Li, J.L., Huang, B.C., Han, C.M., Yuan, C., Sun, M. and Chen, H.L. 2015. A tale of amalgamation of three Permo-Triassic collage systems in Central Asia: Oroclines, sutures, and terminal accretion. *Annu. Rev. Eearth Pl. Sc.,* **43**, 477-507.

Xu, M.J., Huang, H., Huang, Z.C., Wang, P., Wang, L.S., Xu, M.J., Mi, N., Li, H., Yu, D.Y. and Yuan, X.H. 2018. Insight into the subducted Indian slab and origin of the Tengchong volcano in SE Tibet from receiver function analysis. *Earth Planet. Sci. Lett.,* **482**, 567-579.

Yang, T., Moresi, L., Zhao, D., Sandiford, D. and Whittaker, J. 2018. Cenozoic lithospheric deformation in Northeast Asia and the rapidly-aging Pacific Plate. *Earth Planet. Sci.*

*Lett.,* **492**, 1-11.

Zhang, M., Sun, D., Wang, Y. and Wu, Z. 2019. Fine structure of the 660‐km discontinuity beneath southeastern China. *Geophys. Res. Lett.,* **46**, 7304-7314.

Zhao, D., Hasegawa, A. and Kanamori, H. 1994. Deep structure of Japan subduction zones as derived from local,regional, and teleseismic events. *J. Geophys. Res.,* **99**, 22313-22329.

Zhao, Y., Zhang, Y., Geng, M., Jiang, J. and Zou, X. 2019. Involvement of slab‐derived fluid in the generation of Cenozoic basalts in Northeast China inferred from machine learning. *Geophys. Res. Lett.,* **46**, 5234-5242.

Zhu, H., Tian, Y., Zhao, D., Li, H. and Liu, C. 2019. Seismic structure of the Changbai intraplate volcano in NE China from joint inversion of ambient noise and receiver functions. *J. Geophys. Res.,* **124**, 4984-5002.

Zhu, L. 2000. Crustal structure across the San Andreas Fault, southern California from teleseismic converted waves. *Earth Planet. Sci. Lett.,* **179**, 183-190.

Zhu, L. and Kanamori, H. 2000. Moho depth variation in southern California from teleseismic receiver functions. *J. Geophys. Res.,* **105**, 2069-2980.

**Figure's captions:**

Fig. 1. Left panel: location of the study region. Inset: distribution of events used in this study; blue dots: events collected from permanent seismic stations; red dots: events collected from the YP temporary seismic network; green dots: events collected from the XI

temporary seismic network. Right panel: Tectonic framework of NE China. Black triangles: permanent seismic stations, blue triangles: YP temporary seismic network, green triangles: XI temporary seismic network; a-f: profiles of P-wave velocity perturbation and CCP stacking of receiver functions (the locations are the same as those in a previous receiver function study (He, 2019); g-l: CCP stacking profiles of receiver functions. WDL: Wudalianchi volcano region, CBS: Changbaishan volcano zone. White lines: tectonic boundaries.

Fig. 2. CCP stacking profiles of the receiver functions (a-f). Blue rectangle: deepened region of the 410 km discontinuity and elevated region of the 660 km discontinuity at the centres of profiles c and d. The dataset was resampled and calculated with stacked amplitudes 2000 times by employing the bootstrapping method, and the final mean receiver functions corresponding to the 95% confidence level were calculated (Fig. S3). 410 km and 660 km are the upper mantle discontinuities, respectively.

Fig. 3. P-wave perturbation profiles overlain on CCP stacking profiles of receiver functions (profiles e and f of Fig. 2; for the locations of the profiles, please see Fig. 1).

Fig. 4. CCP stacking profiles (g-l). The dataset was resampled and calculated with stacked amplitudes 2000 times by employing the bootstrapping method, and the final mean receiver functions corresponding to the 95% confidence level were calculated (Fig. S5). 410 km and 660 km are the upper mantle discontinuities.

Fig. 5. Piercing points at depth of the 410 km (a) and depth of the 660 km (b), as calculated by the 1-D AK135 velocity model (Kennett et al., 1995). The piercing points are reasonably distributed at depths of 410 and 660 km (a and b). The numbers of stacking amplitudes at the 410 km discontinuity (c) and 660 km discontinuity (d), which are greater than 100. Depths of the 410 km discontinuity (e) and 660 km discontinuity (f) and the MTZ thickness (g). Depths of the 410 and 660 km discontinuities and the MTZ thickness after correction on the basis of a 3-D global P- and S-wave velocity model (Lu et al., 2019) and removal of the effects of velocity heterogeneities in the upper mantle. The dataset was resampled and calculated with stacked amplitudes 2000 times by employing the bootstrapping method, and the final mean receiver functions corresponding to the 95% confidence level were calculated. WDL: Wudalianchi volcano region; CBS: Changbaishan volcano zone.

Fig. 6. Depths of the 410 km discontinuity (a) and 660 km discontinuity (b) and the MTZ thickness (c), which have been corrected on the basis of a local 3-D velocity model (He and Santosh, 2016) and have had the effects of velocity heterogeneities in the upper mantle removed. The number of stacking amplitude points is greater than 100. The dataset was resampled and calculated with stacked amplitudes 2000 times by employing the bootstrapping method, and the final mean receiver functions corresponding to the 95% confidence level were calculated. WDL: Wudalianchi volcano region; CBS: Changbaishan volcano zone.

Fig. 7. Distribution of the crustal thickness (a) and Vp/Vs ratio (b) (He and Santosh, 2016).

Fig. 8 Model defined in this study. Hollow arrow: migration direction of the upwelling mantle plume. Dashed line: original location of the upwelling mantle plume in the Mesozoic.

**Author contributions**

H.C. conducted the analysis, interpreted the results and wrote the manuscript.

**Additional information**

Competing Interests: The author declares no competing interests.

**Electronic supplementary material**

Supplementary Information

**Figure 1.**

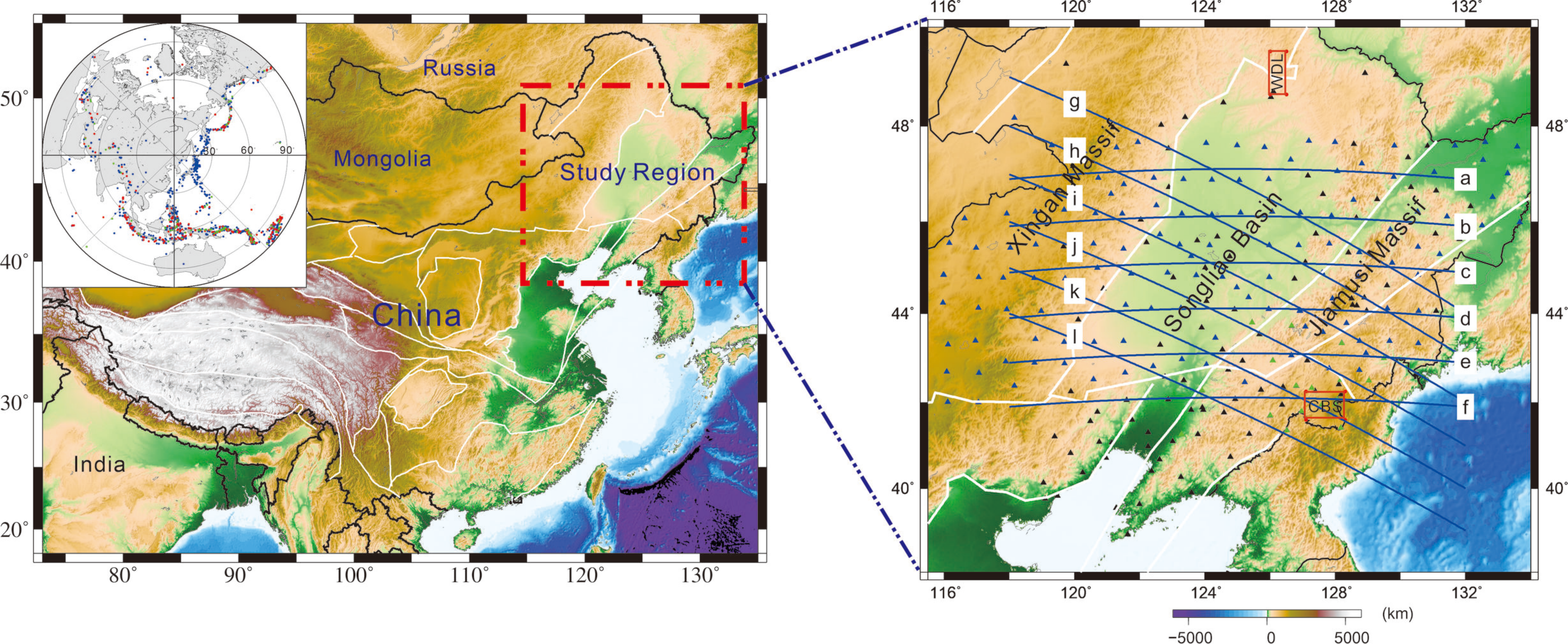

Russia
Mongolia
Study Region
China
India
80°
90°
100°
110°
120°
130°
20°
30°
40°
50°
60
90
116°
120°
124°
128°
132°
48°
44°
40°
Xingan Massif
Songliao Basin
Jiamusi Massif
WDL
CBS
a
b
c
d
e
f
g
h
i
j
k
l
(km)
−5000
0
5000

**Figure 2.**

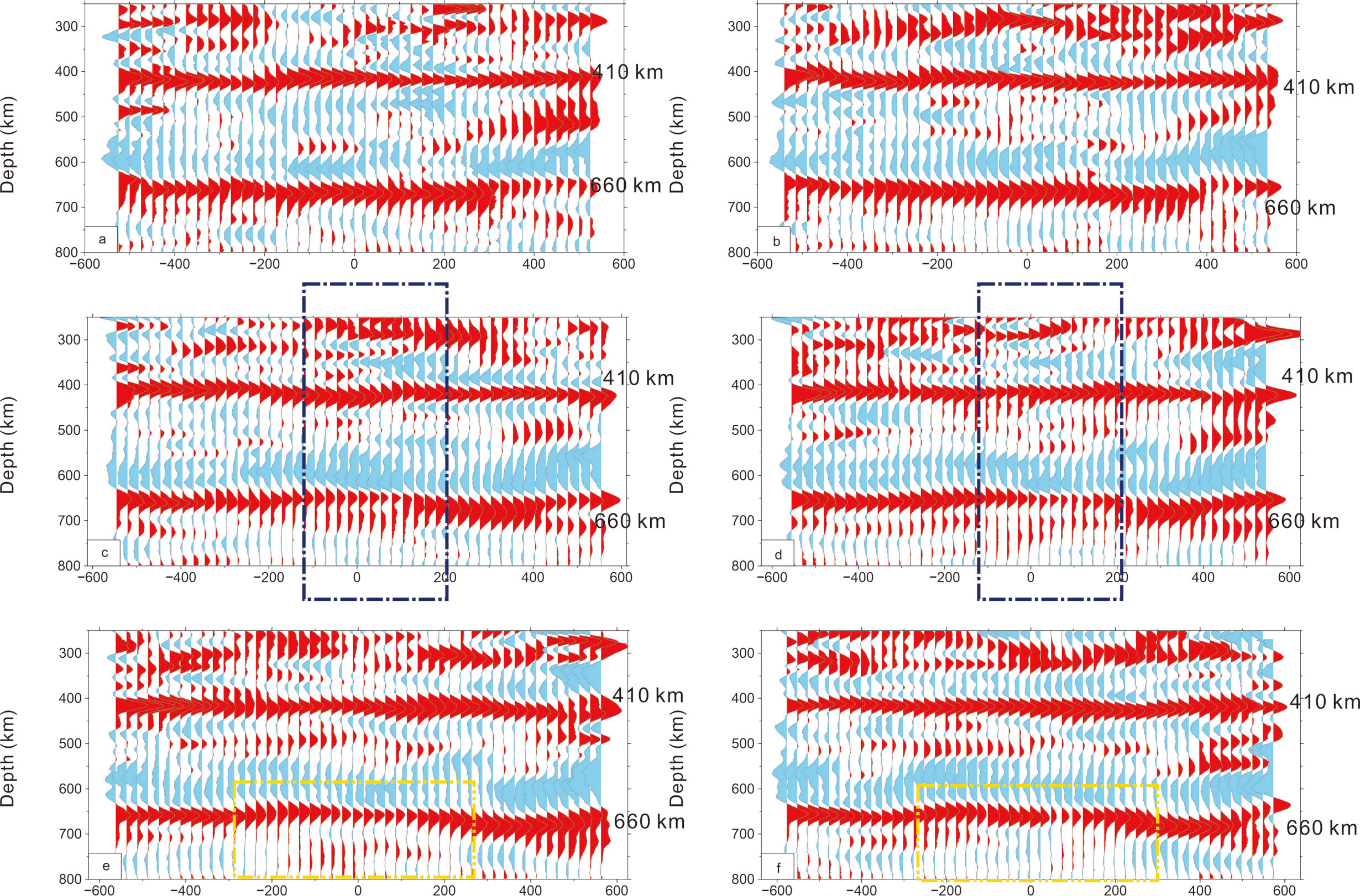

a
b
c
d
e
f
Depth (km)
410 km
660 km
300
400
500
600
700
800
-600
-400
-200
0
200
400
600

**Figure 3.**

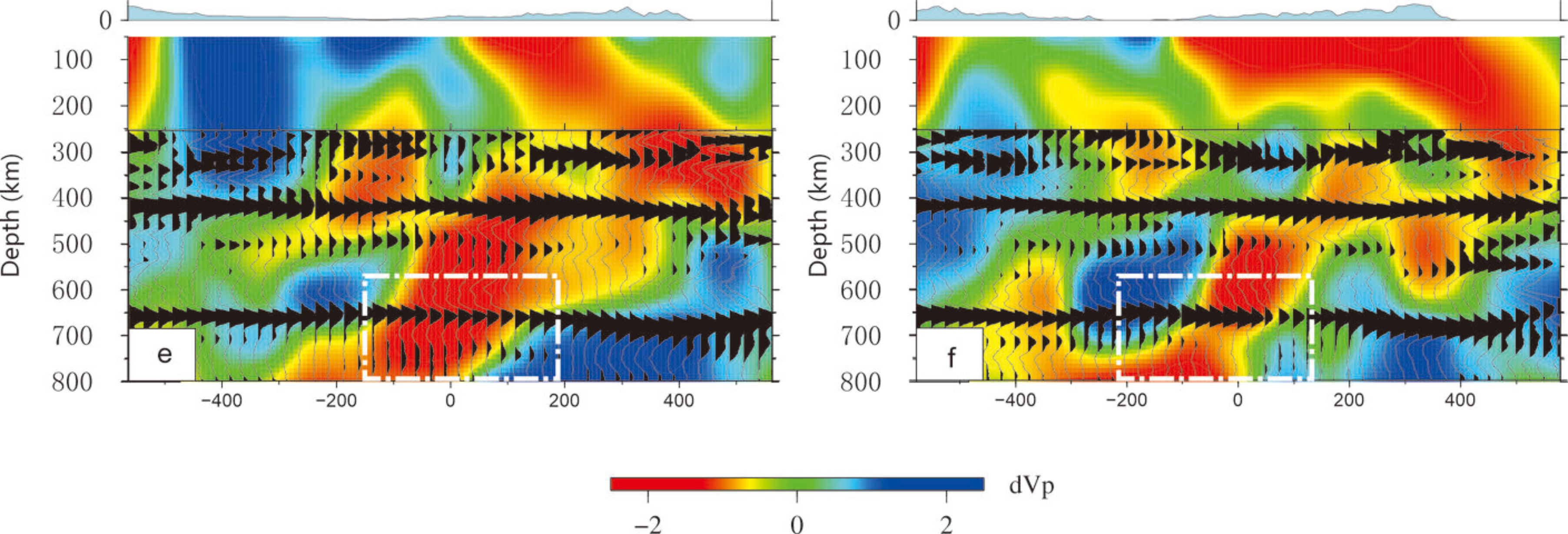

0
100
200
300
400
500
600
700
800
Depth (km)
e
-400
-200
0
200
400
0
100
200
300
400
500
600
700
800
Depth (km)
f
-400
-200
0
200
400
dVp
−2
0
2

**Figure 4.**

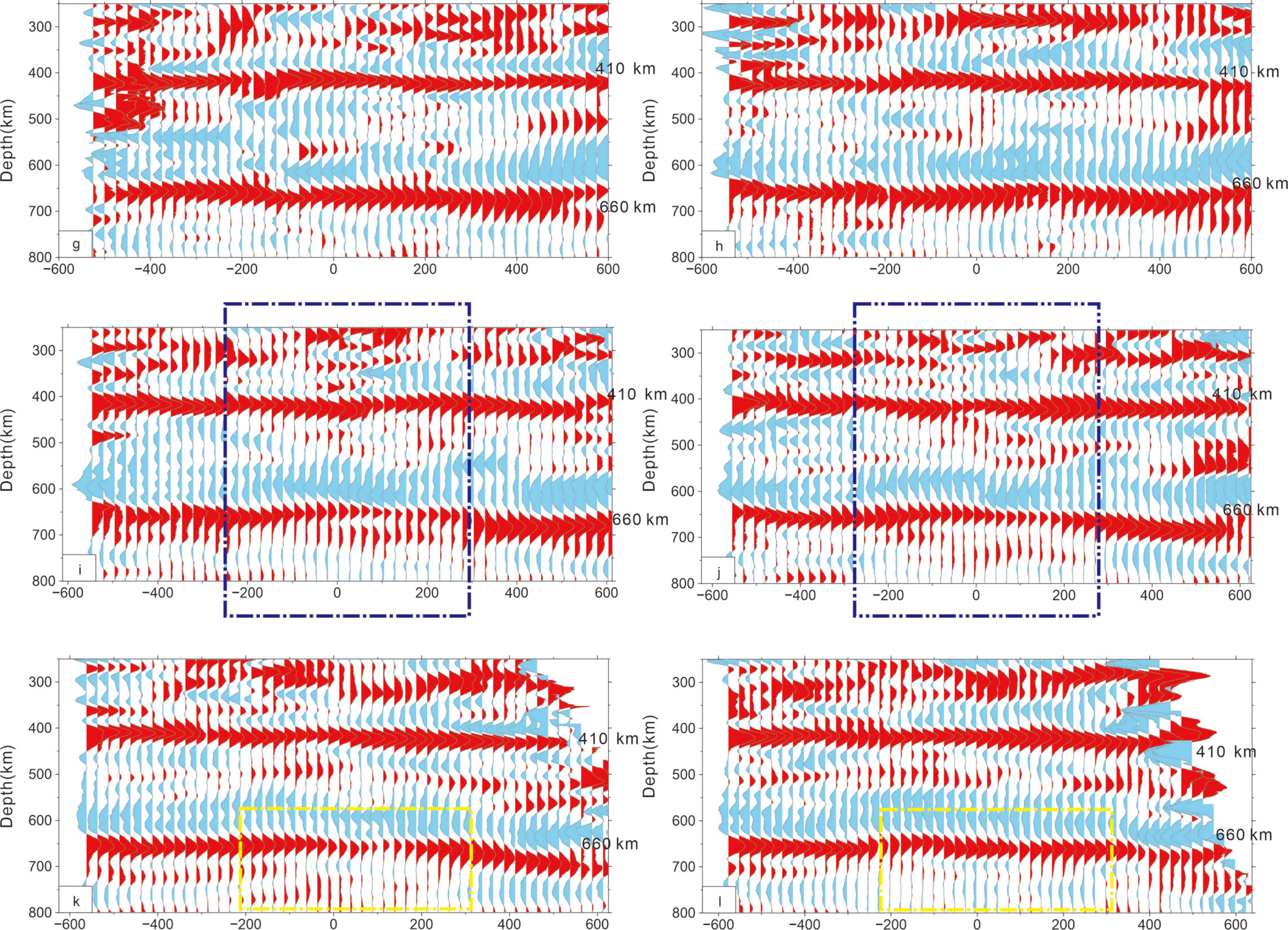

Depth(km)
410 km
660 km
g
h
i
j
k
l
-600
-400
-200
0
200
400
600
300
400
500
600
700
800

**Figure 5.**

a
b
c
d
e
f
g
Songliao Basin
CBS
WDL
(km)
−5000
0
5000
Count
200
400
600
800
360
390
420
660
690
240
270
300
116°
120°
124°
128°
132°
40°
44°
48°

**Figure 6.**

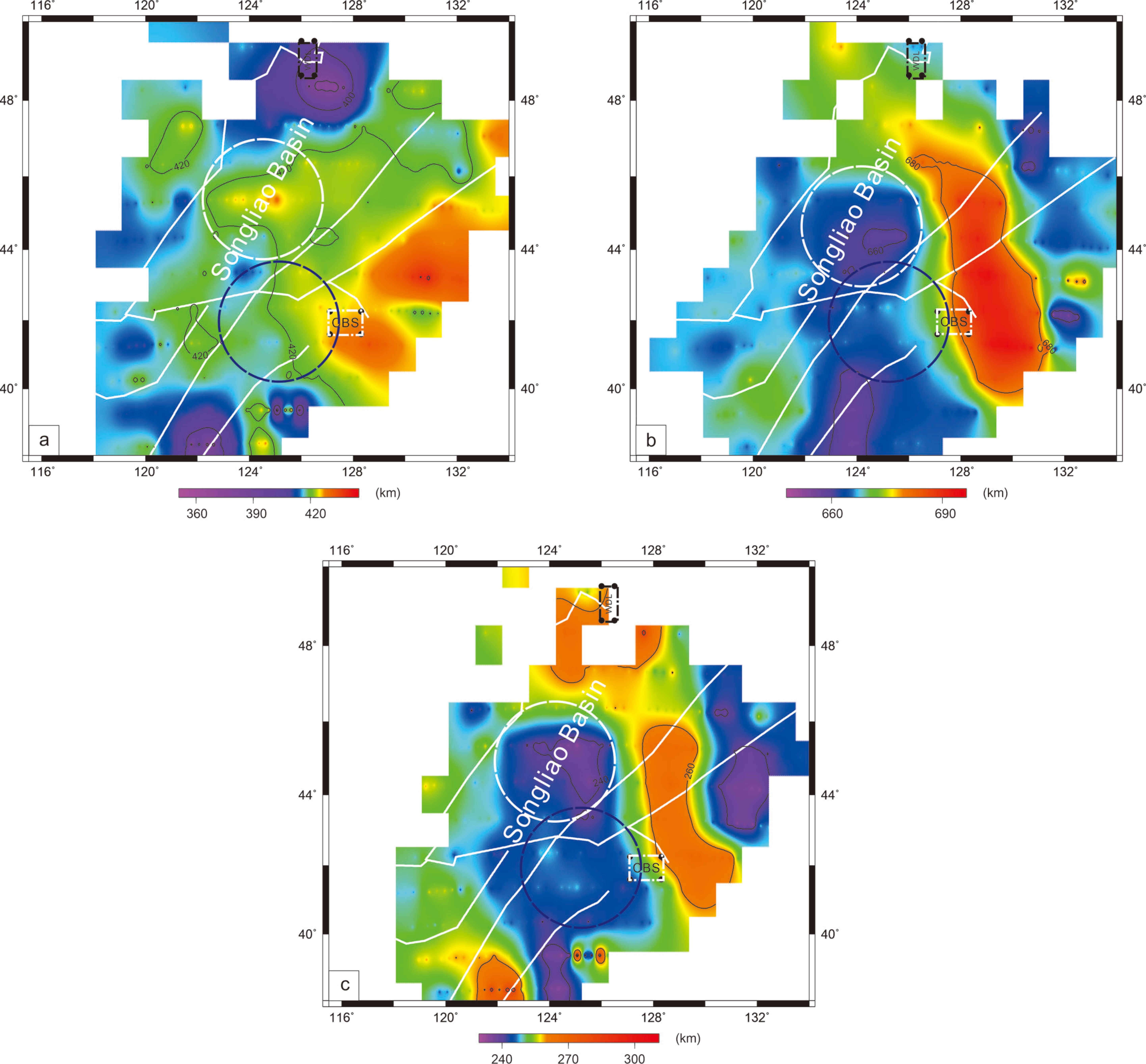
116°
120°
124°
128°
132°
48°
44°
40°
Songliao Basin
WDL
CBS
420
400
a
360
390
420
(km)
b
680
660
690
c
260
240
270
300

**Figure 7.**

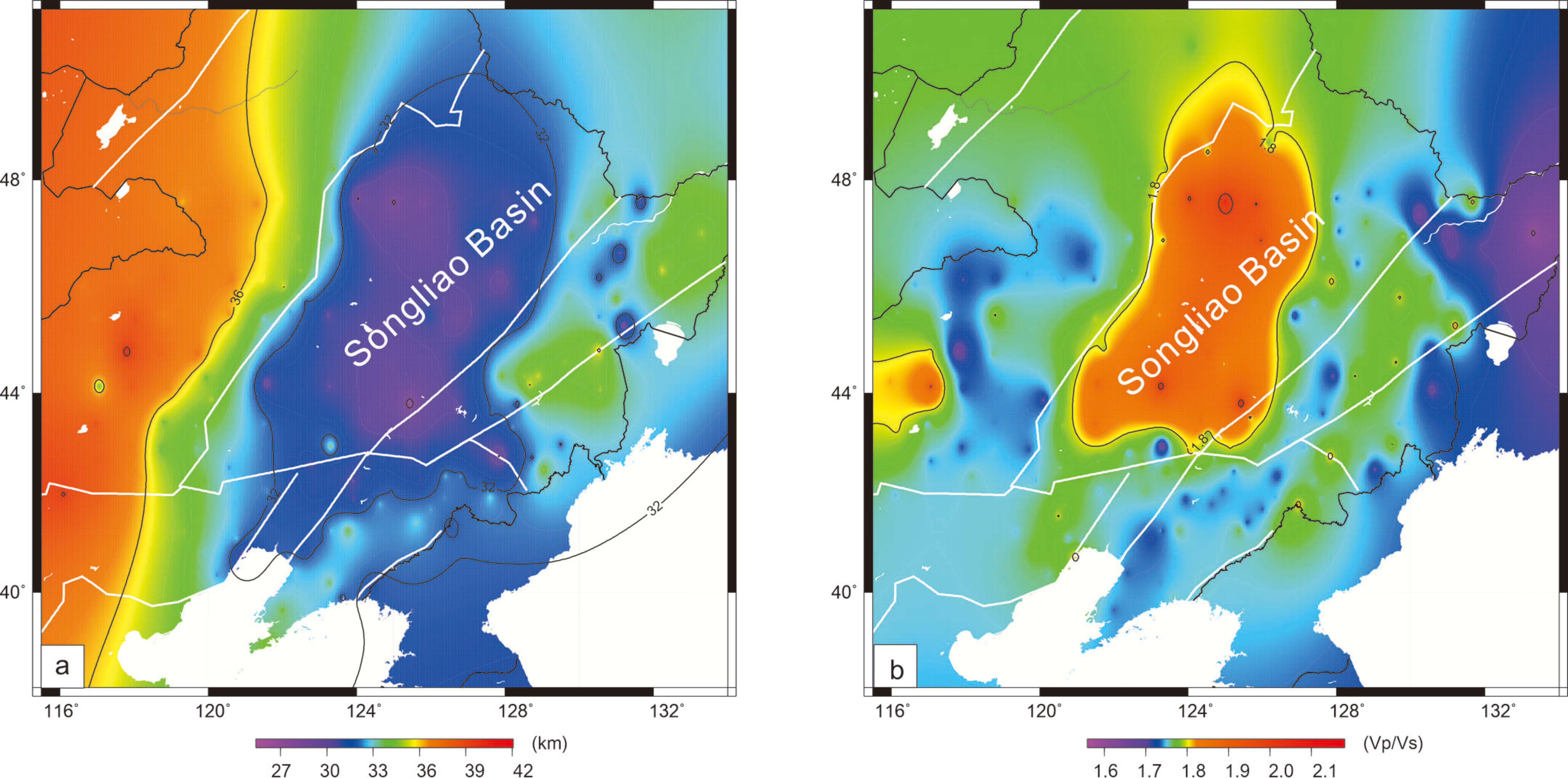

a
Songliao Basin
36
32
48°
44°
40°
116°
120°
124°
128°
132°
(km)
27
30
33
36
39
42
b
Songliao Basin
1.8
48°
44°
40°
116°
120°
124°
128°
132°
(Vp/Vs)
1.6
1.7
1.8
1.9
2.0
2.1

**Figure 8.**

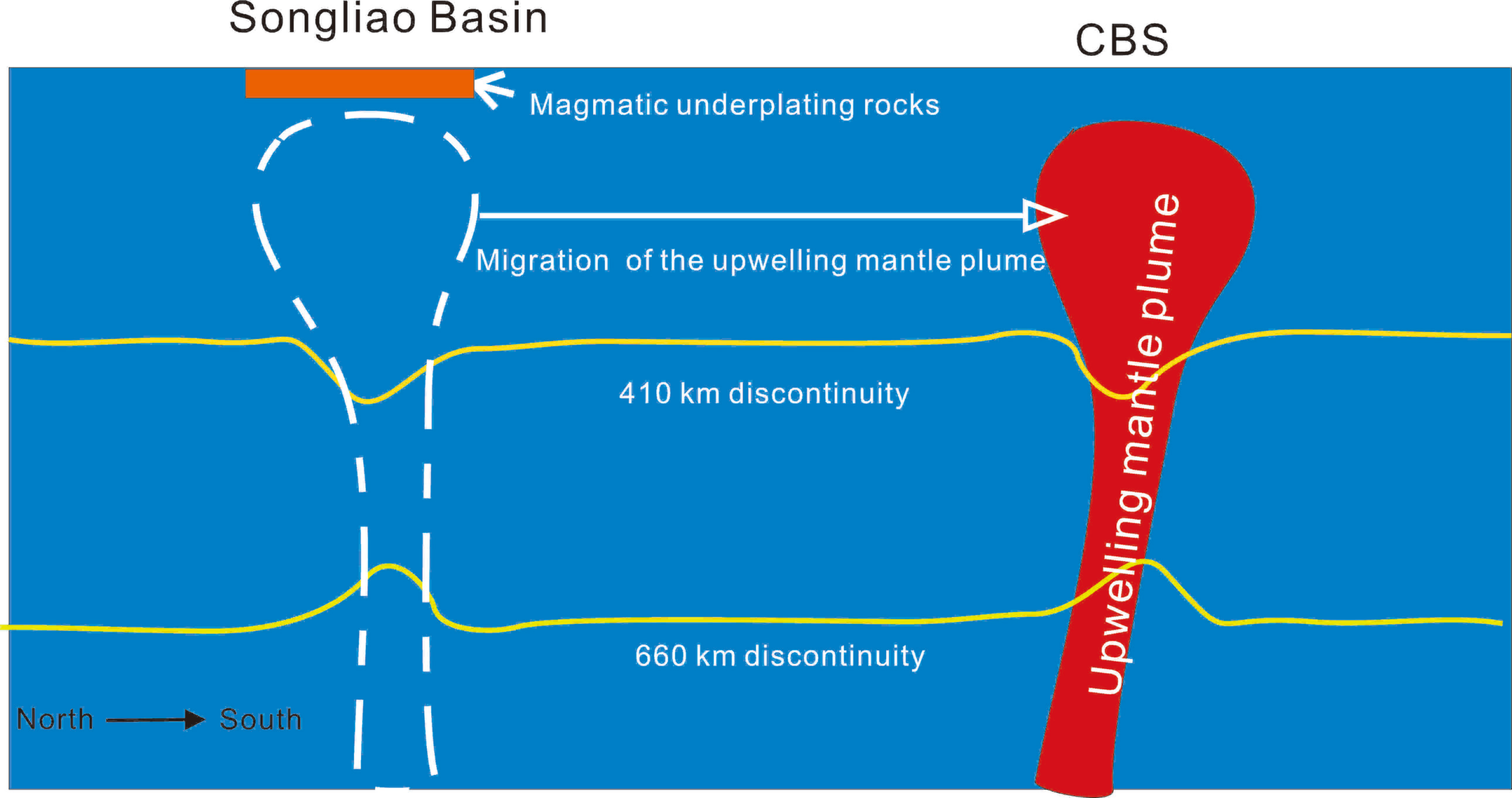
Songliao Basin
CBS
Magmatic underplating rocks
Migration of the upwelling mantle plume
Upwelling mantle plume
410 km discontinuity
660 km discontinuity
North
South